



Gupta, V., Alam, F., Verma, P., Kannan, A.M. and Kumar, S. (2021) Additive manufacturing enabled, microarchitected, hierarchically porous polylactic-acid/Lithium iron phosphate/carbon nanotube nanocomposite electrodes for high performance Li-Ion batteries. *Journal of Power Sources*, 494, 229625.

(doi: [10.1016/j.jpowsour.2021.229625](https://doi.org/10.1016/j.jpowsour.2021.229625))

This is the Author Accepted Manuscript.

There may be differences between this version and the published version. You are advised to consult the publisher's version if you wish to cite from it.

<https://eprints.gla.ac.uk/233425/>

Deposited on: 5 February 2021

**Additive manufacturing enabled, microarchitected, hierarchically porous polylactic-acid/Lithium iron phosphate/carbon nanotube nanocomposite electrodes for high performance Li-Ion batteries**

Vinay Gupta<sup>c</sup>, Fahad Alam<sup>c</sup>, Pawan Verma<sup>c,d</sup>, A. M. Kannan<sup>e</sup>, S. Kumar<sup>a,b,c,\*</sup>

<sup>a</sup>James Watt School of Engineering, University of Glasgow, Glasgow, G12 8LT, UK

<sup>b</sup>Glasgow Computational Engineering Centre, University of Glasgow, Glasgow, G12 8LT, UK

<sup>c</sup>Department of Mechanical Engineering, Khalifa University of Science and Technology, Masdar Campus, Abu Dhabi 54224, UAE

<sup>d</sup>Artie McFerrin Department of Chemical Engineering, Texas A&M University, College Station, TX 77840, USA

<sup>e</sup>The Polytechnic School, Ira A. Fulton Schools of Engineering, Arizona State University, Mesa, AZ, 85212, USA

**ABSTRACT**

The growing need for higher capacity, faster charging-rate, longer cycle-life, and less expensive Li-ion batteries (LIBs) requires architected cathodes and novel manufacturing strategies. Herein, we report the charge/discharge performance of microarchitected, hierarchically porous nanocomposite cathodes, composed of biodegradable polylactic-acid (PLA)/LiFePO<sub>4</sub> (LFP)/carbon nanotube (CNT) enabled by 3D printing. We realize LFP/PLA/CNT cathodes with different CNT loadings (3, 5, 7, and 10 wt.%), interconnected porosities (10%, 30%, 50%, and 70%) and thicknesses (100, 200 and 300  $\mu\text{m}$ ) by utilizing in-house nanoengineered filaments. The nanocomposite cathodes exhibit a specific capacity of 155 and 127  $\text{mAh g}^{-1}$  and an areal capacity of 1.7 and 4.4  $\text{mAh cm}^{-2}$  for 100 and 300  $\mu\text{m}$  thick electrodes, respectively, at 0.39  $\text{mA cm}^{-2}$ . Moreover, we observe that the specific capacity of the thicker electrode (300  $\mu\text{m}$ ) enhances from 125 to 151  $\text{mAh g}^{-1}$  without any loss in areal capacity with increase in porosity. The results demonstrate that the effect of thickness on the specific capacity can be negated by engineering desired porosity, and thereby specific and areal capacities can simultaneously be enhanced. The convergence of emerging nanoscale additive manufacturing and the ability to design ever-more-tightly controlled nano- and micro-architected hierarchical structures will enable the creation of high-performance LIBs.

**KEYWORDS:** 3D printing; PLA; Lithium iron phosphate; Carbon nanotube; Li-ion battery; Specific capacity

**\*Corresponding Author. Email address: [s.kumar@eng.oxon.org](mailto:s.kumar@eng.oxon.org) (S. Kumar)**

## 1. INTRODUCTION

Additive manufacturing (AM) (aka 3D printing) has become a widespread technology due to its ability to realize complex 3D architectures at different length scales, ease of processing and a relatively lower cost than traditional manufacturing [1–4]. AM technologies directly refer to the processes that build 3D objects by adding material layer-upon-layer using different techniques such as fused filament fabrication (FFF), liquid deposition modeling (LDM), selective laser sintering (SLS), stereolithography (SLA), and electron beam melting (EBM) [5–8]. 3D printing is used to develop numerous functional devices such as wearable electronics [9], biomedical implants [10–13], Li-ion batteries (LIBs) [3-8], etc. LIBs are an essential part of our day-to-day life and are critical for several applications such as cellphones, laptops, , micro-electromechanical systems (MEMS), electric vehicles (HEVs) etc. [14,15]. The specific capacity is a critical performance metric of conventional LIBs and is limited by the thickness of electrodes (20-100  $\mu\text{m}$ ). Thicker electrodes fabricated by the traditional blade-casting technique have lower diffusion of Li across the electrode, resulting in inefficient Li intercalation and thereby exhibiting poor specific energy [14–18]. Moreover, during charge/discharge cycles, the active material gets detached from the current collector, leading to loss of active materials, capacity degradation and premature failure. 3D printing has the potential to create LIBs with thicker electrodes ( $>100 \mu\text{m}$ ) and sufficient amount of active materials, enhancing energy density without affecting the ion diffusion length and power density [19–25,25–29]. Emerging advances in AM enable the development of a new class of micro- and nano-architected cellular composites (multi-phase metamaterials), rendering

more electrochemically active surface area per unit geometrical area (specific exchange area) and thereby more specific capacity [23,30].

The first 3D printed interdigitated LIB reported was based on a paste-extrusion-type printing technique. A highly concentrated slurry of  $\text{LiFePO}_4$  (LFP) and  $\text{Li}_4\text{Ti}_5\text{O}_{12}$  (LTO) nanoparticles was patterned on Au current collectors as cathode and anode, respectively [20]. The total volume was  $< 1\text{mm}^3$  rendering the packaging of these micro LIBs difficult. Later Hu et al. [31] developed a 3D printed Li-Ion interdigitated LIB employing the extrusion-type 3D printing technique, using graphene oxide (GO) mixed with LTO (anode)/LFP (cathode) and obtained a discharge capacity of  $91\text{mAh g}^{-1}$  (Areal capacity:  $1.64\text{mAh cm}^{-2}$ ) with a mass loading of  $\sim 18\text{mg cm}^{-2}$ . Lewis et al. [19] further reported a high areal capacity of  $4.45\text{mAh cm}^{-2}$  at  $0.14\text{mA cm}^{-2}$  for fully 3D printed LIBs. Shen et al. [32] 3D printed sulfur copolymer-graphene architectures for Li-S Batteries. 3D printed hierarchically porous frameworks for sodium storage based on graphene/ $\text{Na}_3\text{V}_2(\text{PO}_4)_3$  composites as Na-Ion battery cathode showed high specific capacity and excellent cyclic stability [33]. Recently, Saleh et al. [34] demonstrated an exceptionally high specific capacity and areal capacity for a 3D printed hierarchically porous silver micro-lattice electrode materials. Wang et al. used metal oxide frameworks (MOFs) based 3D printed electrodes for fabricating thicker electrodes ( $>100\text{ }\mu\text{m}$ ) [19]. However, electronic/ionic transport is difficult through thicker electrodes limiting their realizable discharge capacity [17,35]. Therefore researchers have used highly porous metal foam as a 3D current collector to achieve high capacity [36]. However, it leads to additional unwanted weight and other challenges such as cracking and delamination/adhesion issues [37] during charge/discharge cycling [38]. Hou et al.[39] developed flexible electrochemical energy storage devices for addressing the critical issues such as performance degradation, safety,

the need for versatile form factors and compact device integration. Furthermore, Xia's group provided useful insights into engineering of the surface/interface of carbon current collectors, and revolutionized the traditional design of wearable electronics, transcending these devices beyond their current limitations [40]. In the present study, a biodegradable polylactic acid (PLA)-a renewable thermoplastic polymer, is employed as the binding framework for LFP. It is 'processed' from the starch of plants such as corn, sugar cane, and sugar beet, making it environmentally friendly and sustainable. Herein, the design, fabrication, and electrochemical performance of microarchitected 3D printed thick cellular composite cathode made of LFP with PLA and carbon nanotubes (CNTs) are reported. By controlling the CNT loading, architecture and engineered porosity, a high specific and areal capacity for a thick electrode (300  $\mu\text{m}$ ) with enhanced performance and cyclability at various C-rates are achieved.

## **2. EXPERIMENTAL DETAILS**

**Materials.** Commercialized multi-walled carbon nanotubes (MWCNTs) with an average diameter of 50  $\mu\text{m}$ , developed by Applied Nanostructured Solutions, LLC through a unique low cost/high volume CVD process are used. Commercial LFP particles of roughly 1 to 15  $\mu\text{m}$  sizes are obtained from MTI corporations, CA, USA. PLA powder (200 mesh) procured from Shenzhen Esun Industrial co. Ltd., China is used. All solvents are of analytical grade and are used as received from Sigma Aldrich. The entire process of PLA/LFP/CNT cellular nanocomposite fabrication (see Figure 1) is as follows.

**PLA/LFP/CNT nanocomposite preparation by solvent casting.** Among the different composite fabrication methods, the solvent casting method ensures a good homogeneity at the

laboratory scale. PLA polymer powder is dissolved into dichloromethane and homogenized by magnetic stirring. Subsequently, an equal amount of LFP is added, and a fixed amount of CNT (from 3 to 10 wt.%, i.e., the ratio of CNT/(PLA+LFP)) is mixed thoroughly. The obtained slurries are cast onto a glass plate by a doctor blade method and the free-standing composite films are obtained after solvent evaporation (see Figure 1).

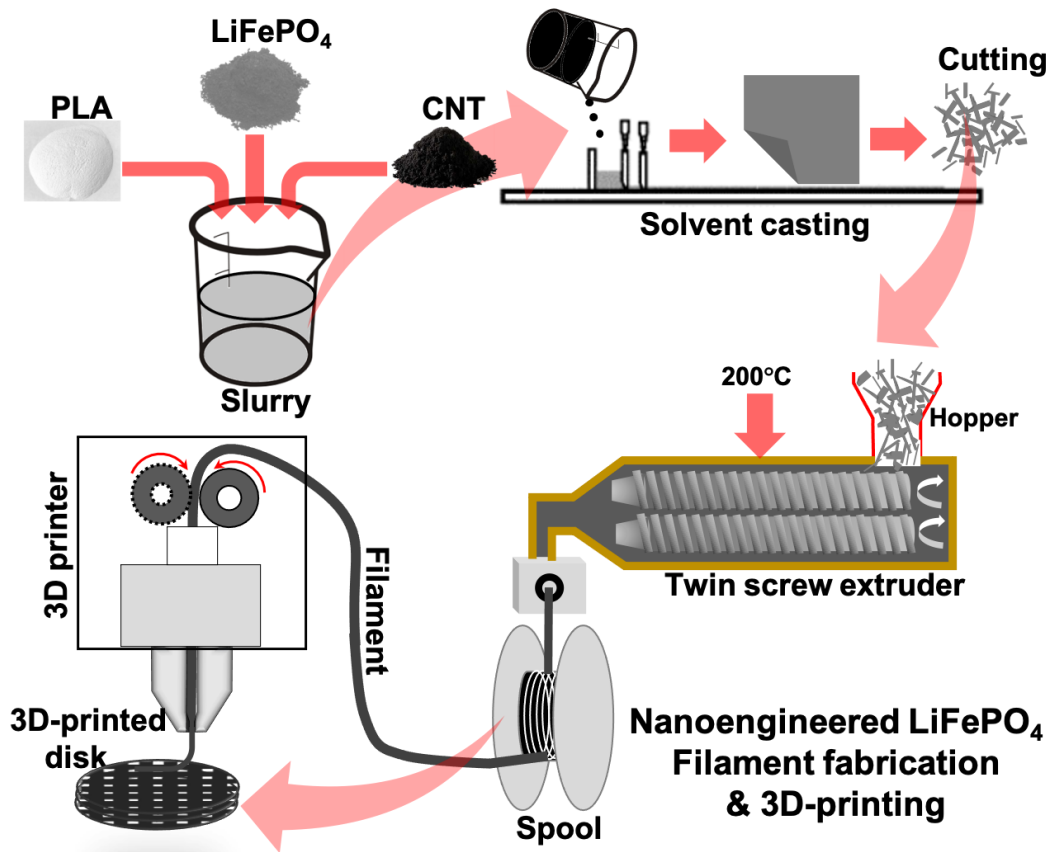


**Figure 1.** Schematic of PLA/LFP/CNT nanocomposite fabrication involving solvent casting, filament extrusion, and 3D printing

**Nanoengineered filament fabrication.** The PLA/LFP/CNT nanocomposite filament feedstock is fabricated by melt mixing extrusion using co-rotating twin-screw micro compounder

(Model: HAAKE MiniLab II). The processing temperature, mixing duration, and screw speed employed are 200 °C, 5 min, and 50 rpm, respectively. Free-standing PLA/LFP/CNT films with various CNT loadings prepared by the solvent casting method are chopped into small pieces and fed into the hopper of the micro compounder. The stepwise details of the filament feedstock development process is shown in Figure 1. Immediately after the exit from the circular die (1.75 mm diameter), the filament is air-cooled and collected.

**3D printing of PLA/LFP/CNT nanocomposites.** Micro-architected cellular composite electrodes are fabricated via fused filament fabrication method utilizing a commercial 3D printer (Creator Pro 3D printer, Flashforge Corporation, Zhejiang, China). The in-house nanoengineered filament (diameter ~1.75 mm) of PLA/LFP/CNT nanocomposite is fed through a pinch roller feed mechanism. The feedstock is then melted and pushed through the nozzle, and the melt is deposited onto a pre-heated print bed surface at the glass transition temperature ( $T_g$ ) of the filament. To achieve desired porosity, in-fill density is varied to 90, 70, 50, and 30% using a slicing tool (Symlify3D software). The micro-architected cellular lattices are fabricated with raster angles 0° and 90° enabling an interconnected porous structure within the circular disk. The default parameters used for the 3D printing of electrodes are summarized in Table S1. The 3D printed micro-architected cellular composite with different CNT loading are named as PLA/LFP/CNT3 for 3 wt.% CNT, PLA/LFP/CNT5 for 5 wt.% CNT, PLA/LFP/CNT7 for 7 wt.% CNT, and PLA/LFP/CNT10 for 10 wt.% CNT.

**Materials Characterization.** The electrodes are characterized by field-emission scanning electron microscope (FESEM) (Hitachi S-4800) and X-ray diffraction (XRD) (Bruker D8 Advance) spectrometer. The electrochemical performance of the 3D printed LFP electrodes is

assessed by fabricating coin cells (CR2032) with Li foil as anode in 1M LiPF<sub>6</sub> dissolved in a mixture of ethylene carbonate, dimethyl carbonate, and diethyl carbonate (volume ratio: 1:1:1). Cyclic voltammetry is evaluated using multi-channel potentiostat/galvanostat (Princeton Applied Research PMC-1000). The constant current charge-discharge performance is evaluated using a battery tester (Maccor Battery Test System Series 4000) in the voltage range 2.5–4.2 V at 25 °C. All impedance measurements are performed with an Autolab PGSTAT 30 instrument (Eco-Chemie, The Netherlands) at 25 °C.

### 3. RESULTS AND DISCUSSION

The XRD patterns of the 3D printed PLA/LFP/CNT cellular nanocomposites with different CNT loadings (Figure S1, supporting information) showed sharper LFP peaks (JCPDS # 811173) without any visible peak of CNT due to intense peaks of LFP with a high order of crystallinity as compared to CNT [41,42]. Hence, Raman analysis is used to confirm the presence of CNT, with stronger D and G bands at 1342 and 1582 cm<sup>-1</sup>, respectively, as shown in Figure S2. The G-band indicates the presence of graphite carbon, whereas the D-band is due to defects or disorders between the CNT graphitic layers. The intensity ratio of D and G bands ( $I_D/I_G$ ) is close to 1 for all the cases. At higher CNT loading, the D and G bands of CNT are much stronger than most of the bands related to PO<sub>4</sub><sup>3-</sup> anions of LFP. For low CNT loading (3 wt.%), bands related to PO<sub>4</sub><sup>3-</sup> anions at 395, 448, 590, 950, 990, and 1042 cm<sup>-1</sup> are observed. The band at 950 cm<sup>-1</sup> is attributed to the intramolecular symmetric vibrations of PO<sub>4</sub><sup>3-</sup> anion (Ag mode of  $\nu_1$ ). Since it is the strongest peak of LFP, it can be observed at high CNT loading and the other peaks at 990 and 1042 cm<sup>-1</sup> are due to the asymmetric stretching modes of the PO<sub>4</sub><sup>3-</sup> anion ( $\nu_3$ ). The Raman bands observed between

400 and 800  $\text{cm}^{-1}$  are the bending modes of  $\text{PO}_4^{3-}$  anion. The Fe-O stretching bands at 215 and 279  $\text{cm}^{-1}$  are also observed [43].

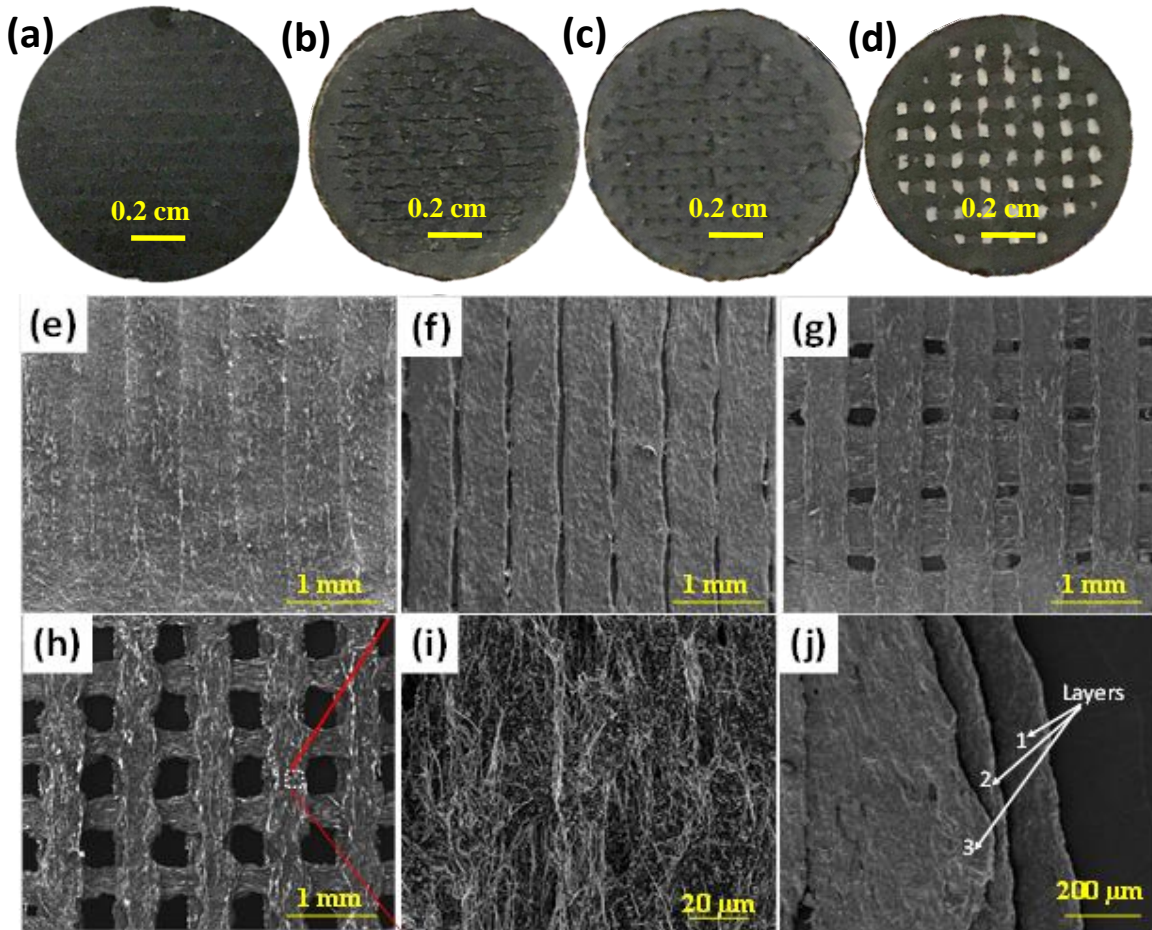


**Figure 2.** 3D printed PLA/LFP/CNT10 cellular nanocomposite (300  $\mu\text{m}$  thickness): Optical and SEM images with porosity (a, e) 10%, (b, f) 30%, (c, g) 50% and (d) 70%. SEM images with porosity. (i) Magnified image of nanocomposite for 70% porosity (j) a 3-layer architecture of cellular nanocomposite.

Figure 2(a-d) shows the optical images of the 3D printed 300  $\mu\text{m}$  thick PLA/LFP/CNT10 cellular nanocomposites comprising three layers (100  $\mu\text{m}$  each) with engineered porosity of 10, 30, 50, and 70%, respectively. The SEM images of PLA/LFP/CNT10 with 10, 30, 50, and 70% porosity are shown in Figure 2(e-h). An ordered square pattern of pores within the circular disc of 1 cm

diameter is enabled via FFF AM by varying the pore size to achieve a desired porosity (10 to 70%) as shown in Figure 2(e-h); the microarchitected cellular nanocomposite exhibiting a grid-like pattern of pores can be clearly observed. The width of a ligament is  $\sim 500 \mu\text{m}$ , and the spacing between the ligaments is varied up to 1 mm to obtain the desired porosity in 100, 200, and 300  $\mu\text{m}$  thick electrodes.

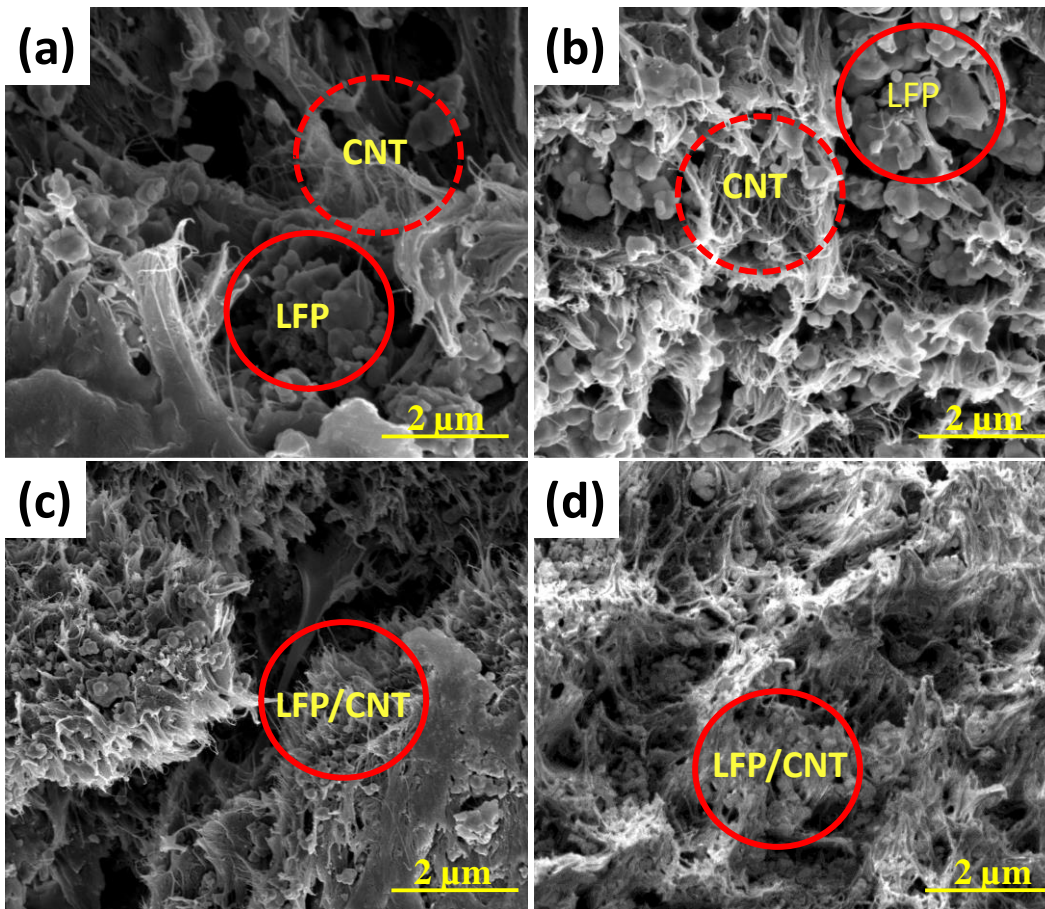


**Figure 3.** High resolution SEM images (cross-sectional) of 3D printed PLA/LFP/CNT cellular nanocomposites with (a) 3, (b) 5, (c) 7, and (d) 10% CNT loading.

Even though the pores are not seen for cellular composites with 10% porosity (Figure 2e), the porous architecture is visible in cellular composites with 30, 50, and 70% porosity, as shown in Figures 2(f-h). Evidently, the well-controlled geometry led to the realization of porosity up to 70%,

which in turn facilitates electrolyte access into the bulk structure of the thick electrodes. A high-resolution SEM image in Figure 2i shows that the ligament has parallel structured CNTs affirming a dense material loading. With a minimum thickness of 100  $\mu\text{m}$  for a single layer, cellular nanocomposite disks up to 300  $\mu\text{m}$  thickness are fabricated by printing three architected layers, as shown in Figure 2j. The low-resolution and high-resolution cross-sectional SEM images of a single layer of PLA/LFP/CNT composites with different wt.% of CNT loading are shown in Figure S3 and Figure 3(a-d). As seen in Figure 3a (Figure S3a), the LFP nanoparticles are not fully coated on to CNTs due to its lower content (i.e., 3wt.% CNT). For 5wt.% CNT loading, there are still several isolated pockets of LFP (Figure 3b and Figure S3b). For 7wt.% CNT loading, the uniformity of loading of LFP around CNTs increases significantly (Figure 3c and Figure S3c), yet the most effective case is 10wt.% CNT loading (Figure 3d and Figure S3d), where LFP is uniformly wrapped around CNTs with much-improved packing density, which is crucial for efficient charge transfer. The nano size gaps between the CNT bundles make the structure hierarchically porous, facilitating electrolyte penetration for maximizing active material utilization.

The elemental mapping is carried out to confirm the uniform distribution of the LFP and CNTs in the cellular composite (Figure S4 and S5). A close-up SEM image of the surface of a ligament of PLA/LFP/CNT cellular nanocomposite (Figure S4a), shows aligned CNTs with LFP nanoparticles wrapped around. It indicates that the LFP particles adhere tightly to the CNT structure, enabling efficient charge transfer. The distribution of carbon, oxygen, phosphorus, and iron are shown in the EDX mapping (Figure S4(b-e)). The EDX spectra (Figure S4f) further confirms the presence of carbon, oxygen, phosphorus, and iron. Moreover, a large area elemental mapping (Figure S5)

confirms that the LFP is homogeneously distributed throughout the ligament. The corresponding elemental composition is summarized in Table S2.

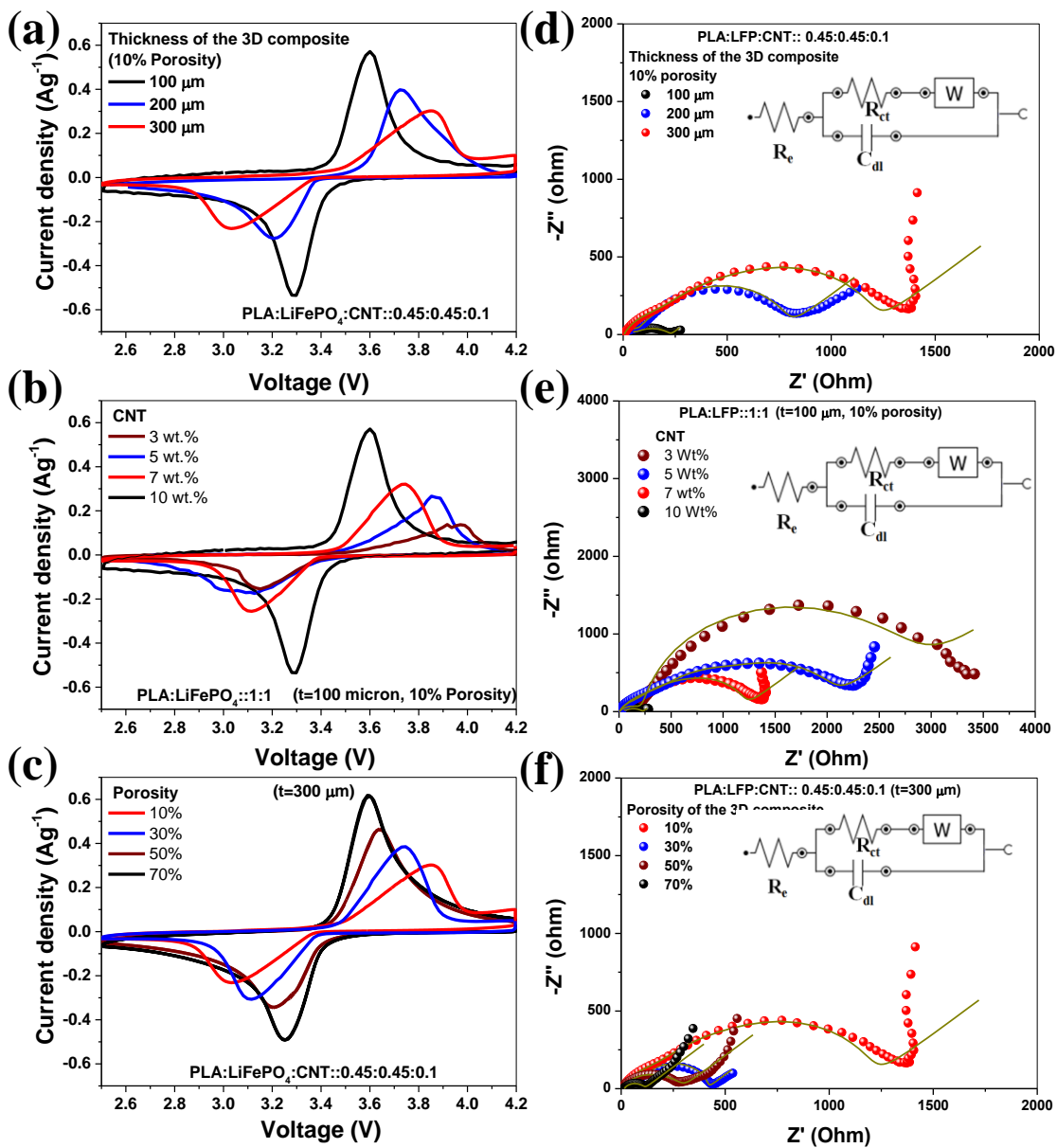


**Figure 4.** (a-c) Cyclic voltammetry and (d-f) Impedance curves of 3D printed PLA/LFP/CNT nanocomposite electrodes based lithium cells. (a, d) for different thicknesses, (b, e), for different wt.% of CNT loading, and (c, f) for different porosities

The electrochemical performance of microarchitected, 3D printed PLA/LFP/CNT nanocomposites are tested via cyclic voltammetry (CV). Figure 4 shows the CV curves at  $0.1 \text{ mV s}^{-1}$  and Nyquist plots for electrodes fabricated with different wt.% of CNTs, porosities, and thicknesses at ambient temperature. The well-defined, sharp redox peaks in the range of 3.1 to  $-3.9 \text{ V}$  (Figures 4a-c) are attributed to the lithium extraction and insertion into the LFP [19]. The shape of the redox peaks is more symmetric for PLA/LFP/CNT10 (Figure 4a for 10% porosity) with  $100\mu\text{m}$  thickness than those with 200 and  $300\mu\text{m}$  thicknesses, suggesting a higher electrochemical reactivity and lower ohmic resistance. Moreover, the gap between the oxidation and reduction peak for the  $100\mu\text{m}$  thick electrode is  $0.33 \text{ V}$ , whereas it is  $0.52$  and  $0.83\text{V}$  for 200 and  $300 \mu\text{m}$  thick electrodes, respectively (Figure 4a), indicating an increase of polarization with an increase in thickness. This is because, for a thicker electrode, the transport of lithium-ion is more resistive and is consistent with the results of our impedance measurements discussed later. The areas under the anodic and cathodic peaks are similar, indicating that lithium ions are reversibly extracted and inserted into the electrode with the same quantity. The high redox current of LFP indicates good charge-transfer kinetics. Figure 4b shows the CV curves of the PLA/LFP/CNT  $100 \mu\text{m}$  thick electrodes with 10% porosity for different CNT loadings (scan rate  $0.1 \text{ mV s}^{-1}$ ). For 10 wt.% of CNT loading, the oxidation and reduction peaks are symmetric, and the gap between them is  $0.35\text{V}$ . For 7, 5, and 3 wt.% CNT loadings, the peaks are non-symmetric, and the gap is  $0.65$ ,  $0.82$ , and  $0.91\text{V}$ , respectively. It shows that the polarization loss increases with decreasing CNT loading. It is quite clear that higher CNT loading is critical for efficient charge-transfer from LFP to CNT. However, to improve the performance of  $300 \mu\text{m}$  thick electrode (PLA/LFP/CNT10), porosity is increased from 10% to 30, 40 and 70% (see Figure 4c) and the results are astounding as there is a significant improvement in the symmetry and gap between the oxidation and reduction peaks from  $0.83$  to

0.63, 0.44 and 0.34V, respectively. Moreover, the CV curve looks similar to that of the 100  $\mu\text{m}$  thick electrode (Figure 4a).

The LIBs are further analyzed by impedance spectroscopy. The Nyquist plots (Figure 4d-f), can be divided into three parts: the high-frequency region corresponds to the electrolyte resistance  $R_e$ . The combination resistance ( $R_e$ ) at high frequency is due to the ionic resistance of the electrolyte, the intrinsic resistance of active materials, and the contact resistance between the active material and current collector [44]. The medium-frequency region corresponds to the charge-transfer resistance ( $R_{ct}$ ) (the semicircle part). The charge transfer impedance ( $R_{ct}$ ) represents the kinetic resistance of the charge transfer at the boundary between electrodes and electrolytes [45]. The low-frequency region is related to the solid-state diffusion of Li-ions, namely the Warburg impedance  $Z_w$  (the oblique line). The insets of Figure 4 (d-f) show an equivalent circuit that is constructed to analyze the impedance spectra.  $C_{dl}$  is the double layer capacitance [45]. As shown in Figure 4(d-f),  $R_e$  is small and is almost the same for all PLA/LFP/CNT10 electrodes. It is in the range of 2-3  $\Omega$ , but the  $R_{ct}$  of 100  $\mu\text{m}$  thick electrode is 250  $\Omega$  which is smaller than 1370 and 1920  $\Omega$  of 200 and 300  $\mu\text{m}$  thick electrodes, respectively (Figure 4d). The influence of CNT loading on the impedance of 100  $\mu\text{m}$  thick PLA/LFP/CNT electrodes is shown in Figure 4e. The  $R_{ct}$  for CNT loading of 3, 5, 7, 10 wt.% are 3700, 2600, 1550, and 250  $\Omega$ , respectively [19]. The porosity of 300 $\mu\text{m}$  PLA/LFP/CNT10 electrodes is varied from 10, 30, 50 to 70%, and the obtained  $R_{ct}$  values are 1550, 1450, 270 and 100 $\Omega$ , respectively (Figure 4f). The lower resistance of PLA/LFP/CNT electrode for high CNT loading can be attributed to an enhancement in electronic conductivity provided by close contact of LFP with the CNT, which leads to better charge transfer between the

electrolyte and electrode. The enhanced porosity leads to better diffusion of Li into the LFP and provides high-rate capability.

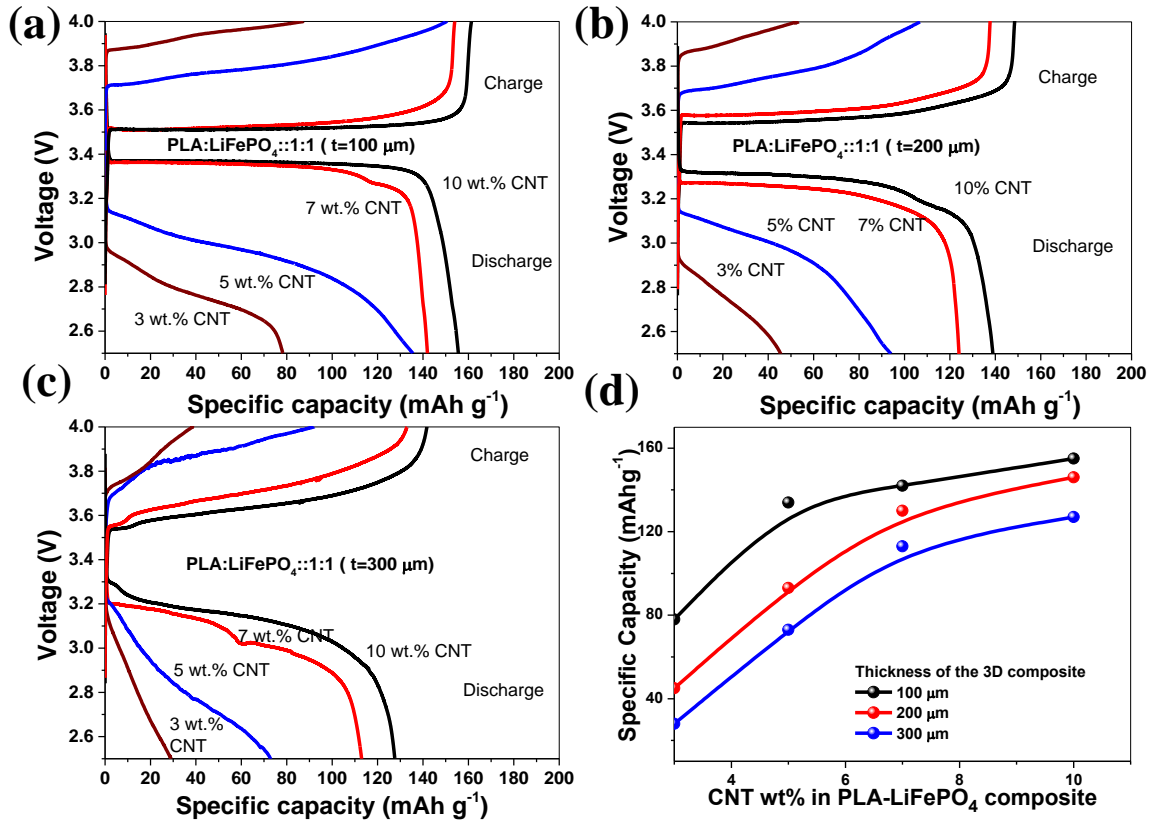


**Figure 5.** Typical charge/discharge voltage profiles of 3D printed PLA/LFP/CNT nanocomposites with 10% porosity and different wt.% of CNT loading at 0.1 C-rate for (a) 100 μm, (b) 200 μm, (c) 300 μm thick electrodes (d) Specific capacity as a function of CNT loading for three different thicknesses.

The rate capability of the 3D printed PLA/LFP/CNT electrodes with various CNT loading and with different thicknesses are further characterized at 0.1C-rate between 2.5 and 4.2 V. The charge-discharge characteristics after ten cycles of PLA/LFP/CNT electrodes are shown in Figure 5. For 100 μm thick electrodes, the discharge capacity is 156, 142, 135, and 78 mAh g<sup>-1</sup> for 10, 7, 5, and 3 wt.% of CNT loading, respectively (Figure 5a). The discharge capacity for the 200 μm thick electrode is 139, 124, 94, and 45 mAh g<sup>-1</sup> for 10, 7, 5, and 3 wt.% of CNT loading, respectively

(Figure 5b). For 300  $\mu\text{m}$  thick electrode, the discharge capacity is 127, 113, 73, and 29  $\text{mAh g}^{-1}$  for 10, 7, 5, and 3 wt.% of CNT loading, respectively (Figure 5c). For lower CNT loading, it is difficult to form an effective electrically conductive network of LFP around CNT (Figure 3), leading to a reduced conducting network and a lower active material utilization. The specific capacity increases with an increase in CNT loading, indicating the role of CNTs in percolation and charge transfer. The highest discharge capacity observed for 10 wt.% CNT loading is 156, 139, and 127  $\text{mAh g}^{-1}$  for 100, 200, and 300  $\mu\text{m}$  thicknesses, respectively. Evidently, the specific capacity decreases with increased electrode thickness due to a decrease in the Li-Ion diffusion. However, the areal capacity corresponding to 10 wt.% CNT loading and 10% porosity for 100, 200, and 300  $\mu\text{m}$  thick electrodes is 1.7, 3.0, and 4.4  $\text{mAh cm}^{-2}$ , respectively. The high areal capacity in the case of thicker electrode exemplifies the merit of microarchitected porous thick electrodes enabled via 3D printing for LIBs as shown in Figure 5d.

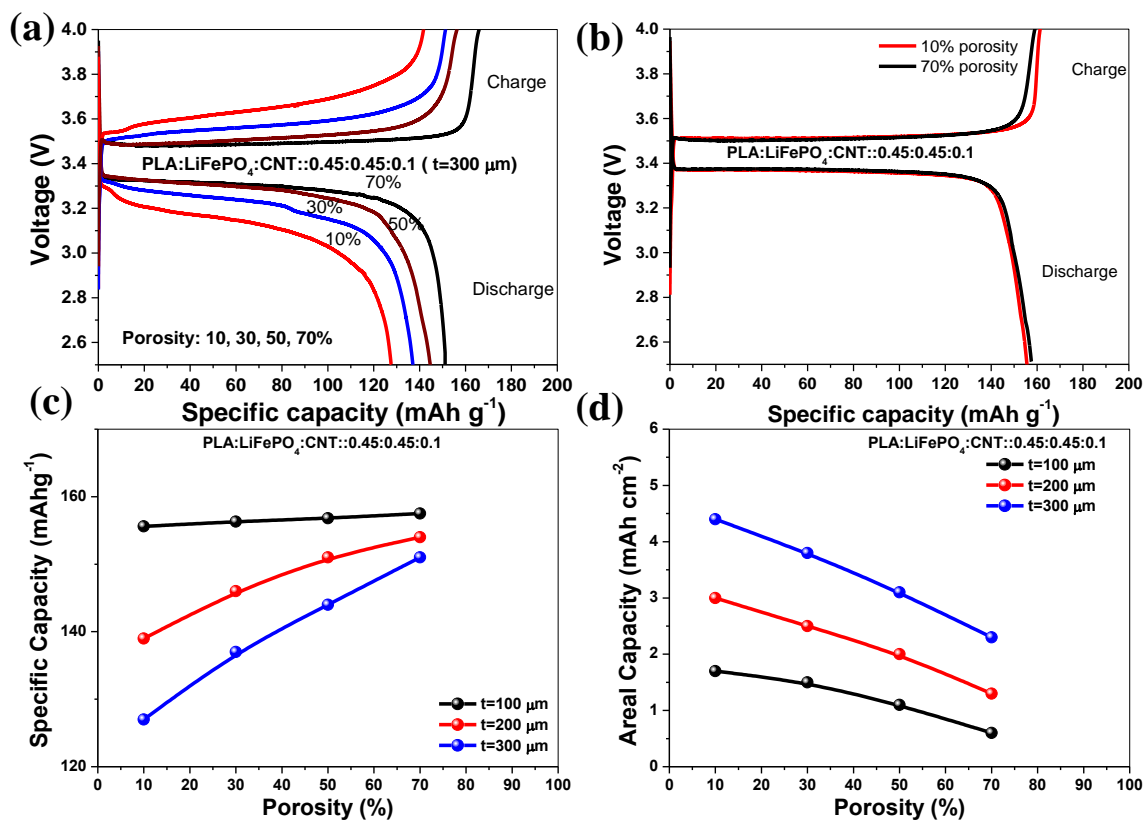


**Figure 6.** Typical charge/discharge voltage profiles (0.1C-rate) of 3D printed PLA/LFP/CNT10 nanocomposites with (a) 300 μm thick electrode with different porosities, (b) 100 μm thick electrode with different porosities (c) Effect of porosity on the specific capacity of the 100, 200 and 300 μm electrodes at 0.1C-rate, (d) Effect of porosity on the areal capacity of the 100, 200 and 300 μm electrodes at 0.1C-rate.

The key objective here is to develop thick electrodes with high specific and areal capacity utilizing the potential of 3D printing to create a porous microarchitecture with tightly controlled geometry. To improve the specific capacity of 300 μm thick electrode, a microarchitected porous network is engineered into the nanocomposite electrodes. In the case of 300 μm electrode (Figure 6a), the discharge capacity increased from 127 for 10% porosity to 137, 145 and 151 mAh g<sup>-1</sup> for 30, 50 and 70% porosity, respectively (Figure 6c), which is close to that of 100 μm thick electrode (156 mAh g<sup>-1</sup>). However, increasing porosity from 10 to 70% in 100 μm electrode does not significantly

increase the specific capacity (Figure 6b). The discharge capacity in 100  $\mu\text{m}$  electrode is increased from 156  $\text{mAh g}^{-1}$  for 10% porosity to 156.3, 156.8, and 157.5  $\text{mAh g}^{-1}$  for 30, 50 and 70% porosity, respectively (Figure 6c). The discharge capacity of 300  $\mu\text{m}$  electrode with 70% porosity is similar to that of 100  $\mu\text{m}$  electrode with 10-70% porosity at 0.1C rate. It is evident that with increasing porosity, the effect of thickness can be negated. It is also observed that there is a significant advantage of porosity at high C-rate, as shown in Figure 7a. The performance of the 300  $\mu\text{m}$  electrode is better than that of 100  $\mu\text{m}$  thick electrode with 62  $\text{mAh g}^{-1}$  and 50  $\text{mAh g}^{-1}$  for 10 C-rates, respectively. The maximum areal capacity corresponding to 10 wt.% CNT loading for 100 (10% porosity) and 300  $\mu\text{m}$  (70% porosity) thick electrodes is 1.7 and 2.3  $\text{mAh cm}^{-2}$ , respectively, which shows that both high specific and areal capacity can be obtained for a thicker electrode. The cycling stability of the 3D printed microarchitected best performing PLA/LFP/CNT10 electrodes is further examined at 0.5 C and 5C. As shown in Figure 7b, both 100 (10% porosity) and 300  $\mu\text{m}$  (70% porosity) electrodes displayed the discharge capacity of around 130  $\text{mAh g}^{-1}$ , with excellent capacity retention. However, at 5C, the 300  $\mu\text{m}$  (70% porosity) electrode exhibits much better specific capacity and capacity retention than that of the 100  $\mu\text{m}$  (10% porosity) electrode due to highly reversible intercalation of Li-ions. The main advantage of 3D printed electrode, in this case, is the ability to realize thicker electrodes with tailored architecture so that at higher C-rate, the insertion and extraction of Li ions can be facilitated by inducing appropriate porosity.

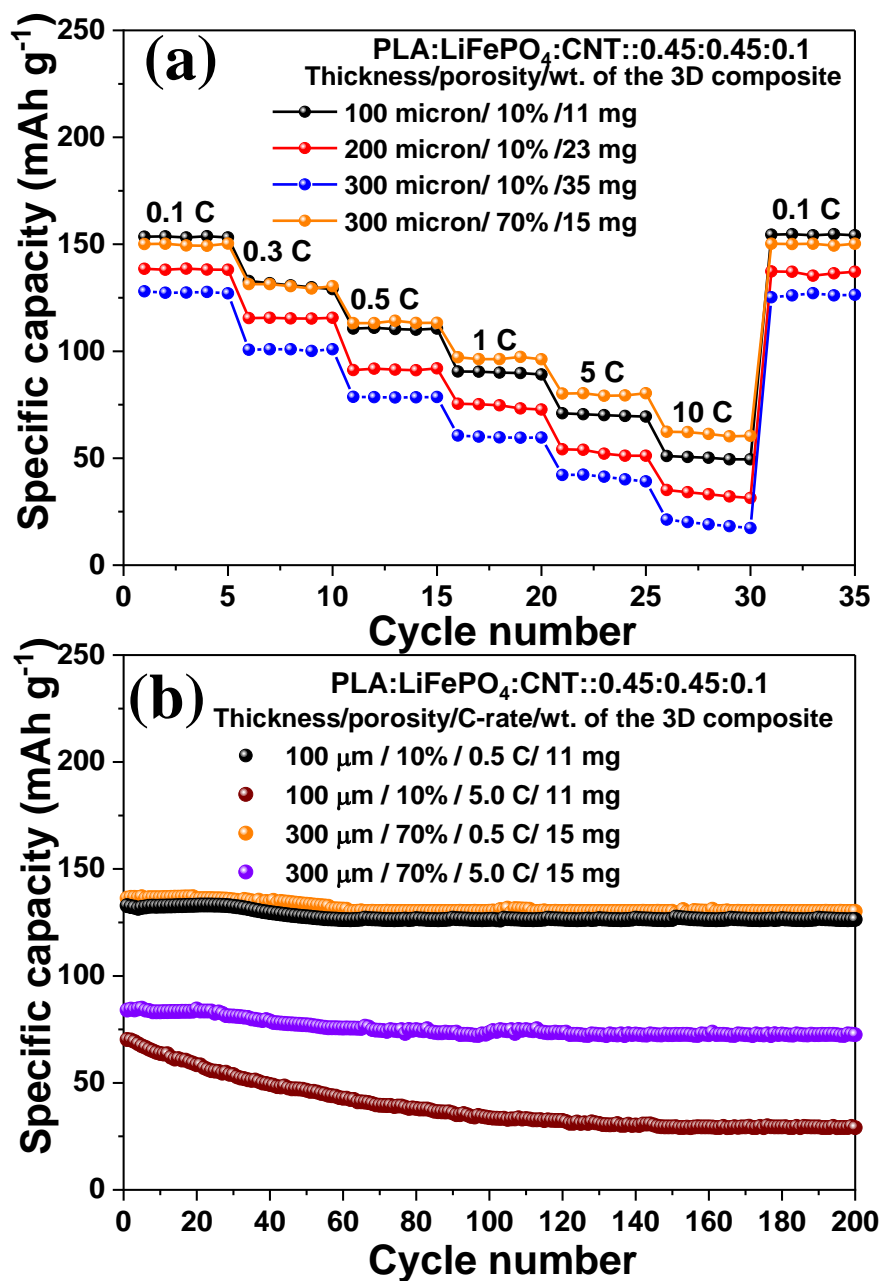


**Figure 7.** (a) Specific capacity of 3D printed PLA/LFP/CNT10 nanocomposite electrodes for different thicknesses and C-rates, (b) Cyclability data for 3D printed PLA/LFP/CNT10 nanocomposite electrodes with different thicknesses at 0.5 and 5C-rates.

To examine the surface morphology of PLA/LFP/CNT10 electrodes with 10% porosity (100 μm) and 70% porosity (300μm), SEM characterization is conducted after 100 charge-discharge cycles

(Figure S6). The low-magnification SEM image (Figure S6a) of the electrode with 10% porosity (100  $\mu\text{m}$ ) shows high roughness with excessive growth of dendritic Li on the entire surface. This is further confirmed at higher magnification (Figure S6b), where loosely stacked Li dendrites and CNTs are observed. A cross-sectional image (Figure S6c) shows degradation of the bulk of the electrode with several cracks. In contrast, the surface of PLA/LFP/CNT10 with 70% porosity (300 $\mu\text{m}$ ) (Figure S6d) remained consistently flat over a large area. The high-resolution image further indicates highly homogenous presence of Li (Figure S6e), and the cross-sectional image (Figure S6f) shows no cracking. This implies that higher porosity leads to stable structure, suppressing dendrite growth during charge-discharge cycling. The coulombic efficiency of the optimized PLA/LFP/CNT10 electrode with better cyclic stability is shown in Figure S7. A coulombic efficiency of 98.4 and 97.6 % is achieved for 70% porosity (300  $\mu\text{m}$ ) and 10% porosity (100  $\mu\text{m}$ ), respectively. The Figure 8 shows that the performance of our 3D printed LIBs is comparable to previous works on 3D printed lithium-ion cells [19,20,31,33,34,34,36,46–57]. Higher specific capacity and coulombic efficiency for 70% porosity (300  $\mu\text{m}$ ) electrode indicate that the appropriate level of engineered porosity can improve the performance of the electrode, particularly at higher C-rate, which is critical for high power applications.

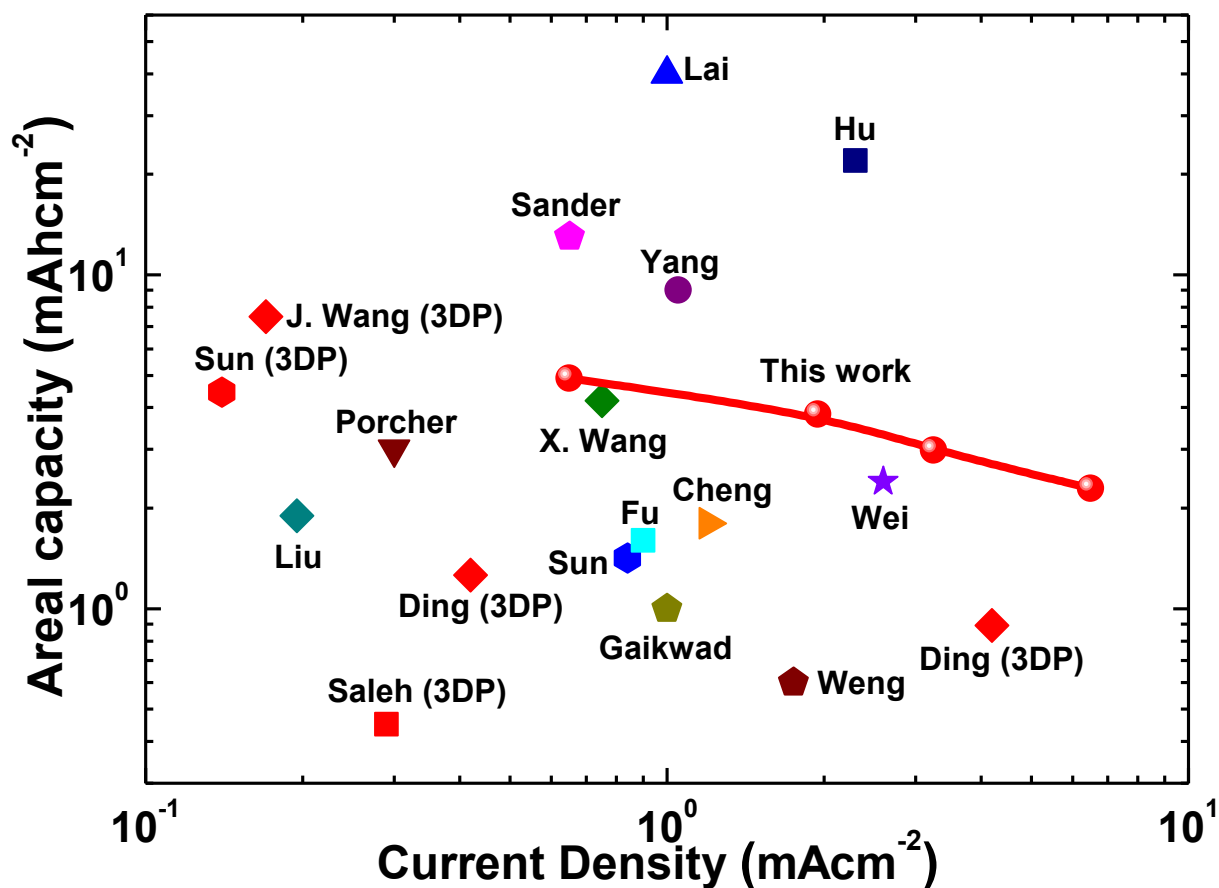


**Figure 8.** Areal capacity as a function of the current density of microarchitected, 3D printed PLA/LFP/CNT coin cell (with 300  $\mu\text{m}$  thick electrode) based LIBs (Red) to extant work. Red markers indicate 3D printed batteries.

#### 4. CONCLUSIONS

Here, we realize three-dimensionally patterned self-supported thick electrodes for high-power-density LIBs via an extrusion-type additive manufacturing technique utilizing in-house nanoengineered filament feedstocks. The 3D printed electrodes comprise interconnected porous LFP frameworks around conducting CNT networks, thereby significantly improve ion and electron transports. The well-designed 3D microstructures of PLA/LFP/CNT10 electrodes with optimized porosity facilitate the electrolyte penetration into the active materials as well as enhanced Li intercalation. The specific capacity of 3D-patterned 300  $\mu\text{m}$  electrodes is 127  $\text{mAh g}^{-1}$  as compared

to 156 mAh g<sup>-1</sup> for thin electrodes (100 μm). However, there is a significant increase in the areal capacity from 1.7 mAh cm<sup>-2</sup> for 100 μm electrode to 4.4 mAh cm<sup>-2</sup> for a 300 μm electrode. Further, the 3D-patterned 300 μm electrode with 70% porosity shows an improved specific capacity of 151 mAh g<sup>-1</sup> while still retaining a high areal capacity of 2.3 mAh cm<sup>-2</sup> and exhibiting remarkable charge-discharge characteristics at higher C-rate compared to 100 μm flat electrodes with 10% porosity. The main drawback in the previous studies is that although there was a significant increase in the areal capacity for thicker electrode, specific capacities are significantly lower. However, we obtain the specific capacity by considering the wt.% of the LFP only, e.g., 0.45 wt.% for PLA:LFP:CNT::0.45:0.45:0.10. Furthermore, we show that a thicker PLA/LFP/CNT electrode with higher porosity and tailored architecture, can exhibit both high specific and areal capacities at high C-rates for high power applications. Clearly, the results demonstrate the potential of additive manufacturing for the development of futuristic Li-ion batteries.

## **AUTHOR INFORMATION**

### **Corresponding Author**

\*E-mail: s.kumar@eng.oxon.org

### **Notes**

The authors declare no competing financial interest

## **ACKNOWLEDGMENT**

The authors thank Abu Dhabi National Oil Company (ADNOC) for the financial support under award no: EX2016-000010.

## References

- [1] I. Gibson, D. Rosen, B. Stucker, *Additive Manufacturing Technologies*, Springer New York, New York, NY, 2015. <https://doi.org/10.1007/978-1-4939-2113-3>.
- [2] B. Berman, 3-D printing: The new industrial revolution, *Business Horizons*. 55 (2012) 155–162. <https://doi.org/10.1016/j.bushor.2011.11.003>.
- [3] J. Liljenherte, P. Upadhyaya, S. Kumar, Hyperelastic strain measurements and constitutive parameters identification of 3D printed soft polymers by image processing, *Additive Manufacturing*. 11 (2016) 40–48. <https://doi.org/10.1016/j.addma.2016.03.005>.
- [4] A.J. Hart, A. Rao, How to print a 3D object all at once, *Science*. 363 (2019) 1042–1043. <https://doi.org/10.1126/science.aaw7062>.
- [5] F. Zhang, M. Wei, V.V. Viswanathan, B. Swart, Y. Shao, G. Wu, C. Zhou, 3D printing technologies for electrochemical energy storage, *Nano Energy*. 40 (2017) 418–431. <https://doi.org/10.1016/j.nanoen.2017.08.037>.
- [6] A. Ambrosi, M. Pumera, 3D-printing technologies for electrochemical applications, *Chemical Society Reviews*. 45 (2016) 2740–2755. <https://doi.org/10.1039/C5CS00714C>.
- [7] M.F. Arif, H. Alhashmi, K.M. Varadarajan, J.H. Koo, A.J. Hart, S. Kumar, Multifunctional performance of carbon nanotubes and graphene nanoplatelets reinforced PEEK composites enabled via FFF additive manufacturing, *Composites Part B: Engineering*. 184 (2020) 107625. <https://doi.org/10.1016/j.compositesb.2019.107625>.
- [8] J. Schneider, S. Kumar, Multiscale characterization and constitutive parameters identification of polyamide (PA12) processed via selective laser sintering, *Polymer Testing*. 86 (2020) 106357. <https://doi.org/10.1016/j.polymertesting.2020.106357>.
- [9] J.A. Lewis, B.Y. Ahn, Three-dimensional printed electronics: Device fabrication, *Nature*. 518 (2015) 42–43. <https://doi.org/10.1038/518042a>.
- [10] S.V. Murphy, A. Atala, 3D bioprinting of tissues and organs, *Nature Biotechnology*. 32 (2014) 773–785. <https://doi.org/10.1038/nbt.2958>.
- [11] B.C. Gross, J.L. Erkal, S.Y. Lockwood, C. Chen, D.M. Spence, Evaluation of 3D Printing and Its Potential Impact on Biotechnology and the Chemical Sciences, *Analytical Chemistry*. 86 (2014) 3240–3253. <https://doi.org/10.1021/ac403397r>.
- [12] F. Alam, K.M. Varadarajan, J.H. Koo, B.L. Wardle, S. Kumar, Additively Manufactured Polyetheretherketone (PEEK) with Carbon Nanostructure Reinforcement for Biomedical Structural Applications, *Adv. Eng. Mater.* 22 (2020) 2000483. <https://doi.org/10.1002/adem.202000483>.
- [13] F. Alam, V.R. Shukla, K.M. Varadarajan, S. Kumar, Microarchitected 3D printed polylactic acid (PLA) nanocomposite scaffolds for biomedical applications, *Journal of the Mechanical Behavior of Biomedical Materials*. 103 (2020) 103576. <https://doi.org/10.1016/j.jmbbm.2019.103576>.
- [14] N. Nitta, F. Wu, J.T. Lee, G. Yushin, Li-ion battery materials: present and future, *Materials Today*. 18 (2015) 252–264. <https://doi.org/10.1016/j.mattod.2014.10.040>.
- [15] K. Shah, N. Balsara, S. Banerjee, M. Chintapalli, A.P. Cocco, W.K.S. Chiu, I. Lahiri, S. Martha, A. Mistry, P.P. Mukherjee, V. Ramadesigan, C.S. Sharma, V.R. Subramanian, S. Mitra, A. Jain, State of the Art and Future Research Needs for Multiscale Analysis of Li-Ion Cells, *Journal of Electrochemical Energy Conversion and Storage*. 14 (2017) 020801. <https://doi.org/10.1115/1.4036456>.
- [16] L. Lu, X. Han, J. Li, J. Hua, M. Ouyang, A review on the key issues for lithium-ion battery management in electric vehicles, *Journal of Power Sources*. 226 (2013) 272–288. <https://doi.org/10.1016/j.jpowsour.2012.10.060>.

- [17] H. Zheng, J. Li, X. Song, G. Liu, V.S. Battaglia, A comprehensive understanding of electrode thickness effects on the electrochemical performances of Li-ion battery cathodes, *Electrochimica Acta*. 71 (2012) 258–265. <https://doi.org/10.1016/j.electacta.2012.03.161>.
- [18] K. Evanoff, J. Khan, A.A. Balandin, A. Magasinski, W.J. Ready, T.F. Fuller, G. Yushin, Towards Ultrathick Battery Electrodes: Aligned Carbon Nanotube - Enabled Architecture, *Advanced Materials*. 24 (2012) 533–537. <https://doi.org/10.1002/adma.201103044>.
- [19] T.-S. Wei, B.Y. Ahn, J. Grotto, J.A. Lewis, 3D Printing of Customized Li-Ion Batteries with Thick Electrodes, *Advanced Materials*. 30 (2018) 1703027. <https://doi.org/10.1002/adma.201703027>.
- [20] K. Sun, T.-S. Wei, B.Y. Ahn, J.Y. Seo, S.J. Dillon, J.A. Lewis, 3D Printing of Interdigitated Li-Ion Microbattery Architectures, *Advanced Materials*. 25 (2013) 4539–4543. <https://doi.org/10.1002/adma.201301036>.
- [21] J. Hu, Y. Jiang, S. Cui, Y. Duan, T. Liu, H. Guo, L. Lin, Y. Lin, J. Zheng, K. Amine, F. Pan, 3D-Printed Cathodes of  $\text{LiMn}_{1-x}\text{Fe}_x\text{PO}_4$  Nanocrystals Achieve Both Ultrahigh Rate and High Capacity for Advanced Lithium-Ion Battery, *Advanced Energy Materials*. 6 (2016) 1600856. <https://doi.org/10.1002/aenm.201600856>.
- [22] R.R. Kohlmeier, A.J. Blake, J.O. Hardin, E.A. Carmona, J. Carpena-Núñez, B. Maruyama, J. Daniel Berrigan, H. Huang, M.F. Durstock, Composite batteries: a simple yet universal approach to 3D printable lithium-ion battery electrodes, *Journal of Materials Chemistry A*. 4 (2016) 16856–16864. <https://doi.org/10.1039/C6TA07610F>.
- [23] X. Tian, J. Jin, S. Yuan, C.K. Chua, S.B. Tor, K. Zhou, Emerging 3D-Printed Electrochemical Energy Storage Devices: A Critical Review, *Advanced Energy Materials*. 7 (2017) 1700127. <https://doi.org/10.1002/aenm.201700127>.
- [24] S. Park, N.S. Nenov, A. Ramachandran, K. Chung, S. Hoon Lee, J. Yoo, J. Yeo, C.-J. Bae, Development of Highly Energy Densified Ink for 3D Printable Batteries, *Energy Technology*. 6 (2018) 2058–2064. <https://doi.org/10.1002/ente.201800279>.
- [25] J.I. Hur, L.C. Smith, B. Dunn, High Areal Energy Density 3D Lithium-Ion Microbatteries, *Joule*. 2 (2018) 1187–1201. <https://doi.org/10.1016/j.joule.2018.04.002>.
- [26] S. Ferrari, M. Loveridge, S.D. Beattie, M. Jahn, R.J. Dashwood, R. Bhagat, Latest advances in the manufacturing of 3D rechargeable lithium microbatteries, *Journal of Power Sources*. 286 (2015) 25–46. <https://doi.org/10.1016/j.jpowsour.2015.03.133>.
- [27] X. Lou, J. Huang, H. Hu, T. Li, B. Hu, Synthesis of 3D “micro-nano-structure”  $\text{LiFePO}_4/\text{C}$  with high-rate capability and high tap density via a water bath process, *Journal of Materials Science: Materials in Electronics*. 26 (2015) 3392–3396. <https://doi.org/10.1007/s10854-015-2845-2>.
- [28] J.W. Long, B. Dunn, D.R. Rolison, H.S. White, Three-Dimensional Battery Architectures, *Chemical Reviews*. 104 (2004) 4463–4492. <https://doi.org/10.1021/cr020740l>.
- [29] X. Gao, Q. Sun, X. Yang, J. Liang, A. Koo, W. Li, J. Liang, J. Wang, R. Li, F.B. Holness, A.D. Price, S. Yang, T.-K. Sham, X. Sun, Toward a remarkable Li-S battery via 3D printing, *Nano Energy*. 56 (2019) 595–603. <https://doi.org/10.1016/j.nanoen.2018.12.001>.
- [30] Q. Wang, Y. Luo, R. Hou, S. Zaman, K. Qi, H. Liu, H.S. Park, B.Y. Xia, Redox Tuning in Crystalline and Electronic Structure of Bimetal–Organic Frameworks Derived Cobalt/Nickel Boride/Sulfide for Boosted Faradaic Capacitance, *Adv. Mater.* 31 (2019) 1905744. <https://doi.org/10.1002/adma.201905744>.
- [31] K. Fu, Y. Wang, C. Yan, Y. Yao, Y. Chen, J. Dai, S. Lacey, Y. Wang, J. Wan, T. Li, Z. Wang, Y. Xu, L. Hu, Graphene Oxide-Based Electrode Inks for 3D-Printed Lithium-Ion Batteries, *Advanced Materials*. 28 (2016) 2587–2594. <https://doi.org/10.1002/adma.201505391>.

- [32] K. Shen, H. Mei, B. Li, J. Ding, S. Yang, 3D Printing Sulfur Copolymer-Graphene Architectures for Li-S Batteries, *Advanced Energy Materials*. 8 (2018) 1701527. <https://doi.org/10.1002/aenm.201701527>.
- [33] J. Ding, K. Shen, Z. Du, B. Li, S. Yang, 3D-Printed Hierarchical Porous Frameworks for Sodium Storage, *ACS Applied Materials & Interfaces*. 9 (2017) 41871–41877. <https://doi.org/10.1021/acsami.7b12892>.
- [34] M.S. Saleh, J. Li, J. Park, R. Panat, 3D printed hierarchically-porous microlattice electrode materials for exceptionally high specific capacity and areal capacity lithium ion batteries, *Additive Manufacturing*. 23 (2018) 70–78. <https://doi.org/10.1016/j.addma.2018.07.006>.
- [35] F. Jiang, P. Peng, Elucidating the Performance Limitations of Lithium-ion Batteries due to Species and Charge Transport through Five Characteristic Parameters, *Scientific Reports*. 6 (2016). <https://doi.org/10.1038/srep32639>.
- [36] G.-F. Yang, K.-Y. Song, S.-K. Joo, Ultra-thick Li-ion battery electrodes using different cell size of metal foam current collectors, *RSC Advances*. 5 (2015) 16702–16706. <https://doi.org/10.1039/C4RA14485F>.
- [37] J.H. Prosser, T. Brugarolas, S. Lee, A.J. Nolte, D. Lee, Avoiding Cracks in Nanoparticle Films, *Nano Letters*. 12 (2012) 5287–5291. <https://doi.org/10.1021/nl302555k>.
- [38] D. Lv, J. Zheng, Q. Li, X. Xie, S. Ferrara, Z. Nie, L.B. Mehdii, N.D. Browning, J.-G. Zhang, G.L. Graff, J. Liu, J. Xiao, High Energy Density Lithium-Sulfur Batteries: Challenges of Thick Sulfur Cathodes, *Advanced Energy Materials*. 5 (2015) 1402290. <https://doi.org/10.1002/aenm.201402290>.
- [39] R. Hou, G.S. Gund, K. Qi, P. Nakhanivej, H. Liu, F. Li, B.Y. Xia, H.S. Park, Hybridization design of materials and devices for flexible electrochemical energy storage, *Energy Storage Materials*. 19 (2019) 212–241. <https://doi.org/10.1016/j.ensm.2019.03.002>.
- [40] T. Liu, M. Zhang, Y.L. Wang, Q.Y. Wang, C. Lv, K.X. Liu, S. Suresh, Y.H. Yin, Y.Y. Hu, Y.S. Li, X.B. Liu, S.W. Zhong, B.Y. Xia, Z.P. Wu, Engineering the Surface/Interface of Horizontally Oriented Carbon Nanotube Macrofilm for Foldable Lithium-Ion Battery Withstanding Variable Weather, *Adv. Energy Mater.* 8 (2018) 1802349. <https://doi.org/10.1002/aenm.201802349>.
- [41] H. Zhang, Y. Chen, C. Zheng, D. Zhang, C. He, Enhancement of the electrochemical performance of LiFePO<sub>4</sub>/carbon nanotubes composite electrode for Li-ion batteries, *Ionics*. 21 (2015) 1813–1818. <https://doi.org/10.1007/s11581-014-1354-2>.
- [42] A.B. Kanagaraj, H. Al Shibli, T.S. Alkindi, R.A. Susantyoko, B.H. An, S. AlMheiri, S. AlDahmani, H. Fadaq, D.S. Choi, Hydrothermal synthesis of LiFePO<sub>4</sub> micro-particles for fabrication of cathode materials based on LiFePO<sub>4</sub>/carbon nanotubes nanocomposites for Li-ion batteries, *Ionics*. 24 (2018) 3685–3690. <https://doi.org/10.1007/s11581-018-2662-8>.
- [43] E. Markevich, R. Sharabi, O. Haik, V. Borgel, G. Salitra, D. Aurbach, G. Semrau, M.A. Schmidt, N. Schall, C. Stinner, Raman spectroscopy of carbon-coated LiCoPO<sub>4</sub> and LiFePO<sub>4</sub> olivines, *Journal of Power Sources*. 196 (2011) 6433–6439. <https://doi.org/10.1016/j.jpowsour.2011.03.059>.
- [44] J.-K. Kim, J. Scheers, Y.-J. Choi, J.-H. Ahn, G.-C. Hwang, Facile preparation of nanoporous and nanocrystalline LiFePO<sub>4</sub> with excellent electrochemical properties, *RSC Advances*. 3 (2013) 20836. <https://doi.org/10.1039/c3ra42516a>.
- [45] C. Liu, F. Xu, X. Cheng, J. Tong, Y. Liu, Z. Chen, C. Lao, J. Ma, Comparative study on the electrochemical performance of LiFePO<sub>4</sub> cathodes fabricated by low temperature 3D printing, direct ink writing and conventional roller coating process, *Ceramics International*. (2019). <https://doi.org/10.1016/j.ceramint.2019.04.124>.
- [46] J. Wang, Q. Sun, X. Gao, C. Wang, W. Li, F.B. Holness, M. Zheng, R. Li, A.D. Price, X. Sun, T.-K. Sham, X. Sun, Toward High Areal Energy and Power Density Electrode for Li-Ion Batteries via Optimized

- 3D Printing Approach, *ACS Applied Materials & Interfaces*. 10 (2018) 39794–39801. <https://doi.org/10.1021/acsami.8b14797>.
- [47] W. Lai, C.K. Erdonmez, T.F. Marinis, C.K. Bjune, N.J. Dudney, F. Xu, R. Wartena, Y.-M. Chiang, Ultrahigh-Energy-Density Microbatteries Enabled by New Electrode Architecture and Micropackaging Design, *Adv. Mater.* 22 (2010) E139–E144. <https://doi.org/10.1002/adma.200903650>.
- [48] L. Hu, F. La Mantia, H. Wu, X. Xie, J. McDonough, M. Pasta, Y. Cui, Lithium-Ion Textile Batteries with Large Areal Mass Loading, *Adv. Energy Mater.* 1 (2011) 1012–1017. <https://doi.org/10.1002/aenm.201100261>.
- [49] J.S. Sander, R.M. Erb, L. Li, A. Gurijala, Y.-M. Chiang, High-performance battery electrodes via magnetic templating, *Nature Energy*. 1 (2016). <https://doi.org/10.1038/nenergy.2016.99>.
- [50] J.S. Wang, P. Liu, E. Sherman, M. Verbrugge, H. Tataria, Formulation and characterization of ultra-thick electrodes for high energy lithium-ion batteries employing tailored metal foams, *Journal of Power Sources*. 196 (2011) 8714–8718. <https://doi.org/10.1016/j.jpowsour.2011.06.071>.
- [51] W. Porcher, B. Lestriez, S. Jouanneau, D. Guyomard, Design of Aqueous Processed Thick LiFePO<sub>4</sub> Composite Electrodes for High-Energy Lithium Battery, *J. Electrochem. Soc.* 156 (2009) A133. <https://doi.org/10.1149/1.3046129>.
- [52] X. Wang, Y. Fan, R. Agung Susantyoko, Q. Xiao, L. Sun, D. He, Q. Zhang, High areal capacity Li ion battery anode based on thick mesoporous Co<sub>3</sub>O<sub>4</sub> nanosheet networks, *Nano Energy*. 5 (2014) 91–96. <https://doi.org/10.1016/j.nanoen.2014.02.005>.
- [53] Q. Cheng, Z. Song, T. Ma, B.B. Smith, R. Tang, H. Yu, H. Jiang, C.K. Chan, Folding Paper-Based Lithium-Ion Batteries for Higher Areal Energy Densities, *Nano Lett.* 13 (2013) 4969–4974. <https://doi.org/10.1021/nl4030374>.
- [54] T.-S. Wei, F.Y. Fan, A. Helal, K.C. Smith, G.H. McKinley, Y.-M. Chiang, J.A. Lewis, Biphasic Electrode Suspensions for Li-Ion Semi-solid Flow Cells with High Energy Density, Fast Charge Transport, and Low-Dissipation Flow, *Adv. Energy Mater.* 5 (2015) 1500535. <https://doi.org/10.1002/aenm.201500535>.
- [55] N. Liu, Z. Lu, J. Zhao, M.T. McDowell, H.-W. Lee, W. Zhao, Y. Cui, A pomegranate-inspired nanoscale design for large-volume-change lithium battery anodes, *Nature Nanotech.* 9 (2014) 187–192. <https://doi.org/10.1038/nnano.2014.6>.
- [56] A.M. Gaikwad, B.V. Khau, G. Davies, B. Hertzberg, D.A. Steingart, A.C. Arias, A High Areal Capacity Flexible Lithium-Ion Battery with a Strain-Compliant Design, *Adv. Energy Mater.* 5 (2015) 1401389. <https://doi.org/10.1002/aenm.201401389>.
- [57] W. Weng, Q. Sun, Y. Zhang, S. He, Q. Wu, J. Deng, X. Fang, G. Guan, J. Ren, H. Peng, A Gum-Like Lithium-Ion Battery Based on a Novel Arched Structure, *Adv. Mater.* 27 (2015) 1363–1369. <https://doi.org/10.1002/adma.201405127>.